Chinese Chemical Letters 34 (2023) 107579

Contents lists available at ScienceDirect

Chinese Chemical Letters

journal homepage: www.elsevier.com/locate/cclet

A DFT study of two-dimensional P_2Si monolayer modified by single transition metal (Sc-Cu) atoms for efficient electrocatalytic CO_2 reduction

Chaozheng He [a], Houyong Yang [a], Xi Fu [b,c,*], Xiaoli Cheng [c], Jiyuan Guo [d], Ling Fu [e,**]

[a] Institute of Environmental and Energy Catalysis, Shaanxi Key Laboratory of Optoelectronic Functional Materials and Devices, School of Materials Science and Chemical Engineering, Xi'an Technological University, Xi'an 710021, China
[b] College of Science, Hunan University of Science and Engineering, Yongzhou 425199, China
[c] Department of Physics, Jishou University, Jishou 416000, China
[d] School of Science, Jiangsu University of Science and Technology, Zhenjiang 212003, China
[e] College of Resources and Environmental Engineering, Tianshui Normal University, Tianshui 741001, China

ARTICLE INFO

Article history:
Received 3 May 2022
Revised 21 May 2022
Accepted 1 June 2022
Available online 3 June 2022

Keywords:
First-principles calculation
Global optimization method
CO_2 electrochemical reduction reaction
Single-atom catalysts
Phosphorus silicon compound

ABSTRACT

In the present work, a stable two-dimensional (2D) P_2Si monolayer was predicted. The monolayer is semimetallic/metallic under the PBE/HSE06 functional and is mechanically isotropic. The stability of the P_2Si monolayer has been proved *via* cohesive energy, mechanical criteria, molecular dynamics simulation, and phonon dispersion respectively, and the monolayer possesses high carrier mobility which is three times that of MoS_2. On the other hand, the catalytic performance of the P_2Si monolayer modified with a single transition metals (M = Sc-Cu) atom for the electrochemical reduction of CO_2 was investigated, and the monolayer can catalyze CO_2 with three constraints: stable molecular dynamics, high migration potential of metal atoms, and suitable band gap for electrocatalyst after metal doping exhibiting excellent catalytic stabilization activity and CRR selectivity. In addition, the reduction product of $V@P_2Si$ is HCOOH with an overpotential as low as 0.75 V, and the most suitable reaction path is $^*CO_2 \rightarrow {}^*CHOO \rightarrow O^*CHOH \rightarrow {}^* + HCOOH$ with the final reduction product HCOOH obtained. As a whole, the above results endow the P_2Si monolayer to be a good 2D material holding great promises for applications in nanoelectronics and CO_2 reduction catalysts.

Two-dimensional (2D) materials, especially single layer 2D materials namely monolayers, have been intensively studied in recent years, and they exhibit unique properties and diverse potential applications in nanoelectronics, optoelectronics, and material science [1–5]. Among various monolayers, graphene, MoS_2, h-BN and black phosphorus are typical. However, graphene is zero-gap, MoS_2 is usually unstable and easily oxidized under normal conditions, h-BN does not have a large bandgap, and black phosphorus is easily oxidated in the air [4,5]. Therefore, searching for a new monolayer became an important content in recent related research.

Compounds on Silicon and Phosphorus elements have attracted attentions in recent years, and in experiments phosphorene and silicene have been prepared [6–8]. There also reported several related works on the combination of phosphorus and silicon elements [9–16]. Dykema *et al.* first studied three types of silicon-phosphorus bonds which are stable in contrast with Si-Si and Si-C bonds [16]. Keizer *et al.* experimentally studied highly phosphorus-doped silicon monolayers and found that 75% of the initial deposited P is confined in a layer with a full width at a half-maximum thickness of 1.0 nm, which means the possibility of the P-Si monolayers [9]. Huang *et al.* theoretically found several semiconducting silicon phosphide monolayers with different chemical compositions, however, they mainly studied the electronic properties of acquired monolayers, in which one monolayer $P2_1/m$ Si_1P_1 is a direct gap semiconductor and other monolayers are indirect gap semiconductors with the band gaps range from 1.0 eV to 3.0 eV [10]. These researches indicate a high possibility of getting stable monolayers of phosphorus and silicon elements [9–16]. For this purpose, we carried out the prediction of monolayers with the different chemical compositions of phosphorus and silicon elements by virtual crystal structure analysis through the particle swarm

* Corresponding author at: College of Science, Hunan University of Science and Engineering, Yongzhou 425199, China.
** Corresponding author.
E-mail addresses: fxhuse@163.com (X. Fu), ful263@nenu.edu.cn (L. Fu).

https://doi.org/10.1016/j.cclet.2022.06.002
1001-8417/

optimization (CALYPSO) algorithm once again [17,18]. A new stable P_2Si monolayer has been acquired, and its structural, electronic, mechanical, and optical properties have been studied and presented accordingly.

On the other hand, effective CO_2 capture and conversion are essential to maintain the planet's carbon balance and alleviate energy shortages [19,20]. The electrochemical CO_2 reduction reaction (CO_2RR) [21,22], which uses electricity generated from solar, wind, geothermal, and nuclear energy under mild conditions, is considered the most promising means of energy conversion as it not only mitigates the increasing concentration of CO_2 in the atmospheric atmosphere but also produces high value-added chemical raw materials [23–25]. However, activation of CO_2 has always required high reaction potentials due to the stability [26,27] of the linear structure of the CO_2 molecule and the difficulty to break C=O bonds [28,29]. In addition, electrocatalytic CO_2RR involves a complex multi-proton electron coupling process to produce the reduction products (C1–C3) [30,31]. As an example, CO_2 can be converted into many chemical intermediates such as formic acid [32], methane [33], methanol [34], ethanol [35], carbon monoxide [36], formate [37].

The loading of metal nanoclusters onto various substrates has received much attentions [38,39]. Over the last few decades, researchers have worked to reduce the size of metal nanoclusters to obtain higher metal atom utilization and higher specific surface area for enhanced catalyst activity. The highest atom utilization for metal clusters is achieved by single-atom catalysts (SACs) [40,41], which are single metal atoms dispersed regularly and stable manner on a substrate material. Many researchers have demonstrated that single-atom catalysts loaded on substrates can be effective as highly active sites exhibiting superior catalytic activity compared to conventional catalysts [42,43]. Therefore in this paper, based on the predicted P_2Si monolayer we further studied its catalytic performance modified with a single transition metals (M = Sc-Cu) atom for the electrochemical reduction of CO_2.

Structure search, structural relaxations, and electronic, mechanical, and optical property calculations within the Perdew-Burke-Ernzerhof (PBE) exchange-correlation of generalized gradient approximation (GGA) [44,45] were performed using the VASP code [46,47]. Due to the elimination of long-range part of the Fock exchange, the hybrid Heyd-Scuseria-Ernzerhof (HSE06) functional was used to determine the band gap [48]. In the HSE06 calculation, a fraction of the exact screened Hartree-Fock exchange was incorporated into the PBE exchange using a mixing parameter $\alpha = 0.25$. The energy cut-off was set as 500 eV and Brillouin zone was sampled using k-points with 0.02 $Å^{-1}$ spacing in the Monkhorst-Pack scheme. The atomic positions were fully relaxed during the structural optimization until the energy of atom converges to up to 1.0×10^{-6} eV and the force of the atom was no more than 0.0001 eV/Å. The first-principles molecular dynamics (FPMD) simulations were carried out with a $4 \times 4 \times 1$ supercell in the canonical ensemble (NVT) at different temperatures up to 1400 K and each simulation lasts for 5 ps with a time step of 0.5 fs. A supercell approach with the supercell size as $5 \times 5 \times 1$ implemented in PHONOPY package was used to acquire phonon dispersion of the monolayer [49].

Global structure searches of P_2Si monolayer were performed with particle-swarm optimization (PSO) method as implemented in the CALYPSO algorithm [17,18]. In the PSO calculations, population size and a number of generations were taken as 30 and 40, as well as the number of layers, the area of 2D structure, and the gap between two labs were accordingly set as MultiLayer = 1, Area = 20, VacuumGap = 12 Å. The key parameters EDIFF, NSW and PSTRESS in INCAR_i ($i = 1, 2, 3$) files were taken as $1e^{-2}$, $1e^{-3}$, $1e^{-5}$, 50, 100, 250 and 0.001, respectively.

All the calculations were performed by the method of spin-polarized density functional theory in the Dmol^3 package [50]. The PBE exchange-correlation functional in the GGA range was used and Grimme's scheme was adopted for long-range dispersion DFT-D correct. An all-electron double numerical atomic orbital augmented by d-polarization functions (DNP) was chosen as the basis set [51]. The solvent effect is included by a conductor-like screening model (COSMO) [52] with a dielectric constant of 78.54.

All the calculations used a 2×3 unit supercell to simulate the endless P_2Si nanosheet. All atoms were fully relaxed without any constraints up to the atomic forces smaller than 0.002 Ha/Å, displacement smaller than 0.005 Å, and the total energy with a convergence threshold of 10^{-6} a.u. The basis-set cutoff was set to 4.1 Å. The vacuum space is set to 20 Å in the z-direction to avoid interactions between periodic images. The Brillouin zone integration was performed on a $5 \times 5 \times 1$ Monkhorst-Pack k-points mesh. The charge distribution was determined by Hirshfeld analysis. Here, we define the adsorption energies (E_{ad}) to describe the interaction between the intermediates of the NO reduction to NH_3 and the P_2Si sheets as:

$$E_{ad} = E_{M\text{-}P_2Si} - E_{P_2Si} - E_M \quad (1)$$

where $E_{M\text{-}P_2Si}$, E_{P_2Si}, E_M represent the total energy of the adsorption of intermediates, pritine P_2Si monolayer, the small molecule during the synthetic route, respectively. Here the complete linear synchronous transit/quadratic synchronous transit (LST/QST) method, with repeated conjugate gradient (CG) refinement to find the minimum energy pathway (MEP) were applied for transition state (TS) searches were performed to acquire the energy barriers of the migration of transition metal atoms on the surface of P_2Si.

Following the work of Rossmeisl *et al.* [53], under the standard reaction condition, the chemical potential of a proton and electron pair ($\mu(H^+ + e^-)$) is equal to half that of gaseous hydrogen ($\mu(H_2)$). For each elemental step, the Gibbs free energies (ΔG) were calculated using the following equation:

$$\Delta G = \Delta E + \Delta ZPE + \Delta H - T\Delta S + \Delta G_{pH} + \Delta G_U \quad (2)$$

where ΔE is the reaction energy based on DFT calculations, ΔZPE is the zero-point energy (ZPE) correction, T is set to 298.15 K, ΔS and ΔH are the entropy and heat capacity change. G_{pH} and U_L are the contributions from the pH and limited electrode potential (U), respectively. U_L is defined as

$$U_L = -neU \quad (3)$$

where n is the number of transferred electrons. G_{pH} is defined as:

$$G_{pH} = -k_B T \ln\left[H^+\right] = pH \times k_B T \ln 10 \quad (4)$$

where k_B is the Boltzmann constant. Here pH was set to zero during the process of calculation. Overpotential can be obtained by calculating the difference between the $U_{equilibrium}$ potential and limit-potential:

$$\eta = U_{equilibrium} - U_L \quad (5)$$

The geometric structure including top and side views of the predicted P_2Si monolayer is shown in Fig. S1 (Supporting information), and its symmetry of space group is P1 with the lattice parameters as $a = 6.101$ Å, $b = 4.11$ Å, $\alpha = 90.0°$, $\beta = 89.9978°$ and $\gamma = 90.0°$ From the figure, each Si atom is tetracoordinate with four P atoms exhibiting four-coordinated sp^3 hybridization. Each P atom bridges two Si atoms realizing two-coordinated sp^2 hybridization. Moreover from the top view, the P_2Si monolayer is composed of 8-membered rings arranged by alternate P and Si atoms and only has one type of bond P-Si with the lengths as 2.23286, 2.23295, 2.23289, 2.23290 Å, which are smaller than those of 2.262 Å in other P-Si monolayers and 2.254 Å in the compound $SiPH_4$ in Ref. [12].

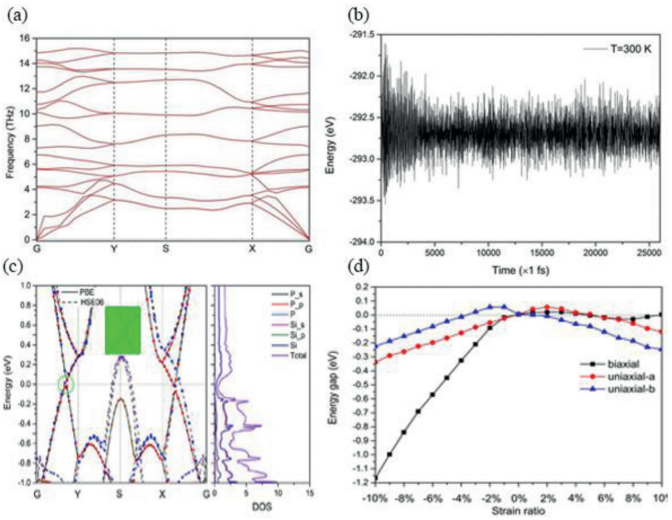

Fig. 1. (a) Phonon dispersion of the P_2Si monolayer. The high-symmetry points are G (0, 0, 0), (b) energy oscillations of the MD simulation at room temperature 300 K. (c) Band structure and density of state (DOS) of P_2Si monolayer. (d) Modulated band gap (PBE) of P_2Si monolayer *versus* the strain ratio.

To show the formation of bonds and charge transfers in the P_2Si monolayer, we calculated the electron localization function (ELF) shown in Fig. S1a and performed bader charge analysis. From the bader analysis, charges being shifted from the Si atom to two P atoms are about 0.8461 |e| and 0.8415 |e|, indicating the formation of P-Si bonds. From the top view in Fig. S1b, there exhibits electron localization between the Si atom and two P atoms, also verifying the formation of P-Si bonds. Moreover, from the side view, there shows huge electron localization around the P atoms which is sp^2 hybrid with three pairs of alone electrons. The sp^2 electronic structures of P atoms provide huge free electrons leading to the semimetallic/metallic property of the P_2Si monolayer [54].

The stability of P_2Si monolayer was examined by calculating its cohesive energy, phonon dispersion, elastic constants, and performing molecular dynamics (MD) simulations respectively. Firstly, the formula of cohesive energy $E_{coh} = (mE_P + nE_{Si} - E_{P_mSi_n})/(m+n)$ was used, where E_P, E_{Si} and $E_{P_mSi_n}$ are total energies of a single P atom, a single Si atom and the monolayer, respectively. The cohesive energy of P_2Si monolayer is calculated as −3.517 eV/atom, which is comparable to some monolayers, such as other Si_xP_y, BP_5, g-BP, and B_2C [10,55,56], and is smaller than that of the experimentally realized 2D silicene and phosphorene [57]. This result verifies the P_2Si monolayer should be a potential stable phase of P-Si compounds.

Secondly, we investigated the dynamic stability of the P_2Si monolayer and calculated its phonon dispersion curve shown in Fig. 1a. From the figure, no imaginary (negative) vibration modes exist, indicating the P_2Si monolayer is thermodynamically stable [5]. Moreover, the slopes of longitudinal acoustic branches are not equal along different directions, such as G-Y and G-X, showing the P_2Si monolayer is anisotropic concerning the in-plane stiffness.

Thirdly, to study the thermal stability of the P_2Si monolayer, molecular dynamics (MD) simulations at different temperatures were performed with a relatively large $3 \times 3 \times 1$ supercell. Through the 20 ps MD simulations up to 1400 K, our simulations showed that the P_2Si monolayer maintained its structural integrity, but seriously distorted at about 1200 K. Fig. 1b shows the energy oscillations of MD simulation at room temperature 300 K with a time step of 1 fs, and the energy is oscillating near the equilibrium state which indicates the monolayer is expected to be experimentally feasible.

Finally, we discussed the mechanical properties of the P_2Si monolayer by computing the elastic constants (C_{ij}). A mechanically stable 2D structure satisfies the Born criteria [58]:

$$C_{11}C_{22} - {C_{12}}^2 > 0, C_{66} > 0 \quad (6)$$

The elastic constants of the P_2Si monolayer were calculated as $C_{11} = C_{22} = 27.210$ N/m, $C_{12} = C_{21} = 8.965$ N/m, and $C_{66} = 28.222$ N/m, which exactly meet the mechanical stability criteria, indicating the P_2Si monolayer is mechanically stable. Then in-plane Young's modulus of P_2Si monolayer can be computed as $Y_x = (C_{11}C_{22} - C_{12}C_{21})/C_{22} = 24.256$ N/m and $Y_y = (C_{11}C_{22} - C_{12}C_{21})/C_{11} = 24.256$ N/m, which are lower than the value of MoS_2 monolayer (~128 N/m) [59]. No difference in Young's modules in different directions manifests that the P_2Si monolayer is mechanically isotropic. Moreover, two Poisson's ratios $\nu_x = C_{21}/C_{22}$ and $\nu_y = C_{12}/C_{11}$ are equal with the value as 0.3295.

Band structure and density of state (DOS) of the P_2Si monolayer are presented in Fig. 1c, showing the monolayer is semimetallic with the band gap of 0.0047 eV at the GGA-PBE level, and the CBM and VBM locate at the point (0.000, 0.3684, 0.000) and (0.3684, 0.000, 0.000), respectively. In order to acquire a more accurate band structure, the HSE06 hybrid functional was used, and the P_2Si monolayer is metallic which renders it a potential 2D material in electrocatalysis and energy storage battery. Moreover, the DOS strengths of P atoms are larger than those of Si atoms, and contributions of *p*-orbital from P and Si atoms are larger than those of *s*-orbital from P and Si atoms. These consequences on the DOS strength are consistent with the results of ELF in Fig. 1c.

We further studied the influences of applying strain which is a common engineering strategy to tune band gaps. In-plane biaxial and uniaxial strains were acquired by adjusting the lattice parameters *a* and *b*, and strain ratio is defined as to:

$$\varepsilon = \Delta a/a \times 100\% \text{ or } \Delta b/b \times 100\% \quad (7)$$

with $\Delta a + a$ and $\Delta b + b$ are strained lattice parameters [54]. Under a strain in the scope of −10% to 10%, the effects of the strain ratio to the band gap of P_2Si monolayer are shown in Fig. 1d. From the figure, the band gap of P_2Si monolayer decreases when stretching or compressing the lattice parameters, and for biaxial and uniaxial cases the P_2Si monolayer can transfer from a semimetal to a metal/an indirect narrow-gap semiconductor or from a metal/an indirect narrow-gap semiconductor to a semimetal. Moreover, the impact of the biaxial strain is larger than those of two uniaxial strains. These results enhance applied opportunity of the P_2Si monolayer in optoelectronics and exhibit potential values on nanoelectronic devices based on strain-engineering techniques [54,60,61].

Given the P_2Si monolayer being semimetallic or semiconducting under a low strain ratio under the GGA-PBE functional, we further calculated carrier effective masses and carrier mobilities μ^{2D} using the following formula

$$\mu^{2D} = \frac{e\hbar^3 C^{2D}}{k_B T m^* m_d E_d^2} \quad (8)$$

where m^* is the effective mass, m_d is the average effective mass, $T = 300$ K, and k_B is Boltzmanns Constant. Moreover, the in-plane stiffness is

$$C^{2D} = \left(\frac{2\partial^2 E}{\partial (\Delta l/l_0)^2} \right) / S_0 \quad (9)$$

where E is total energy, S_0 is the area of optimized structure, and E_d is deformation potential (DP) constant along *x* or *y*-direction.

The carrier mobilities of P_2Si monolayer are shown in Table S1 using the GGA-PBE functional as it can yield good estimations of carrier mobility. From the table, the electron mobilities along the *x* and *y* directions are smaller than the hole mobilities, and the

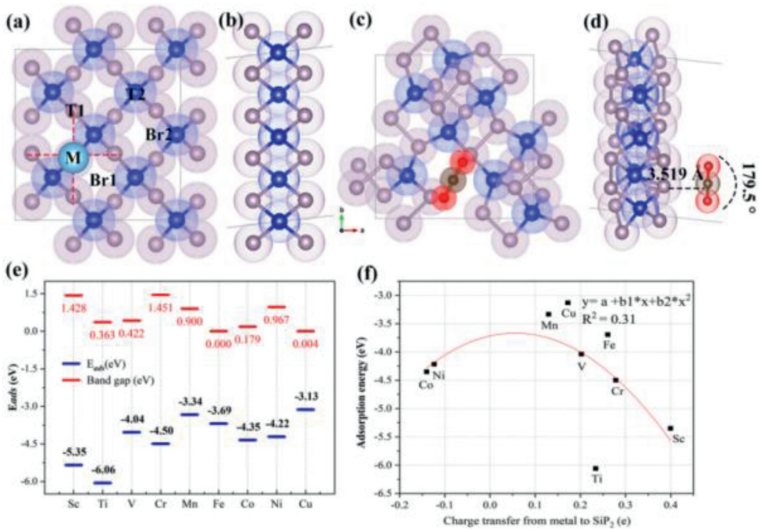

Fig. 2. (a) Structural prototype of the most stable M-P_2Si structure and site of metal atom adsorption. (b) Side view of the P_2Si monolayer. (c, d) The top view and side view of adsorbed CO_2 of pristine P_2Si. (e) The adsorption energies correspond to the most stable adsorption configurations of the 13 kinds of transition metal atoms (Sc-Cu) on the P_2Si surface, and the red short line is the band gap value of P_2Si doped with different metal atoms. (f) The amount of electron transfer between metal atoms and P_2Si after doping different metal atoms.

largest value is 600 $cm^2\ V^{-1}\ s^{-1}$ which is three times that of the MoS_2 monolayer (200 $cm^2\ V^{-1}\ s^{-1}$) [62]. This high hole mobility indicates the P_2Si monolayer can be used as a promising device in the application of nanoelectronics.

Since P_2Si monolayer is a two-dimensional material of a semi-metallic/metallic nature and the presence of uneven ring structure on the P_2Si monolayer facilitates the mosaic of metal atoms, we tried to design a novel CO_2 electrochemical catalyst by single-atom loading. The adsorption sites identified using different chemical environments and the most stable sites tested for transition metal atom loading are shown in Figs. 2a and b, in which the most stable sites are the empty sites in the middle of the four raised P atoms, with M and P4 forming a stable four-ligand pyramidal structure.

As shown in Figs. 2c and d for the most stable configuration of the P_2Si monolayer for CO_2 adsorption, the pure P_2Si monolayer is unable to adsorb CO_2 molecules, and the shortest adsorption distance between CO_2 and the monolayer is 3.519 Å. Moreover, the bond angle of CO_2 molecules is 179.5° meaning no activation degree compared with 180° for gas CO_2 molecules, and the adsorption energy is only −0.11 eV. Therefore, we tried to improve the activation of the catalyst for CO_2 by transition metal atom loading. Firstly, we loaded a single transition metal atom ranging from Sc to Cu on a pure P_2Si monolayer which as the substrate, and selected the single-atom catalyst with the best conductivity and the most stable structure by the adsorption energy, bandgap of the loaded system, ease of migration of metal atoms on the surface [63], and molecular dynamics stability [64], respectively.

Electrocatalysis involves both electrodes and catalysis, so electrocatalysts must meet both requirements: (1) good electrical conductivity for free-electron transfer; and (2) effective activation of the target material [21]. Materials that can conduct electricity cannot always activate the substrate and vice versa. Therefore, a feasible way to design electrocatalysts is to modify the electrodes by employing doping, *etc*. By combining the active component in the form of some chemisorption on the conductive substrate electrode, the dual purpose of both electron transfer and substrate activation can be achieved. Of course, in addition to the consideration of the macroscopic mass transfer factors of the electrode, there is also a problem with the interaction between the modified molecule and the substrate electrode [65], and this interaction needs to be further studied.

Fig. 2e shows bandgaps of the P_2Si monolayer after M loading and the corresponding adsorption energy of M atoms. The stronger adsorption of Sc, Ti, V, Cr, Co, and Ni atoms can be selected according to the requirement of electrocatalyst stability, but at the same time, Ti, V, Mn, and Co atoms should be further selected with the restriction of smaller bandgap if the electrical conductivity is considered. We then studied the number of electrons transferred from the metal atoms to the P_2Si monolayer when the transition metal atoms are loaded on the P_2Si monolayer to form a stable structure. It can be seen from Fig. 2f that Co and Ni atoms prefer to gain electrons from the monolayer (0.140 e and 0.123 e for Co and Ni atoms, respectively), while the other metal atoms tend to transfer electrons to the P_2Si monolayer. In addition, we find an interesting pattern that the ability to lose electrons decreases from Sc to Cu (from left to right in the same period), which is related to the weakening of metallicity.

Figs. S2 and S3 (Supporting information) show side and top views of the most stable structures of the nine transition metal atoms loaded in the P_2Si monolayer. The M metal atoms are chemically bonded to all four P atoms and the bond lengths are in the range of 2.258–2.690 Å, which coincides with the atomic radius of Sc. The above results indicate that the raised fold vacancies on the P_2Si monolayer can anchor the metal atoms tenaciously, and all of them have been chemisorbed. Furthermore, we investigated FPMD simulations of M@P_2Si (M = Sc, V, Cr, Mn) for 2000 ps at 300 K. As shown in Fig. S4 (Supporting information), the structures including Sc, V and Cr atoms are very stable after 2000 ps with no significant changes, but the Mn atom migrates from the P4 vacancy to the bridge position between the two P atoms between the bridge sites. The energy of all four structures oscillates around the equilibrium state, which indicates that the P_2Si monolayer modified by Sc, Cr and V atoms is thermodynamically stable.

However, considering the requirements of conducting performance as an electrocatalyst, the bandgap of M@P_2Si should not be greater than 0.5 eV. But Sc@P_2Si has a bandgap of 1.428 eV, and Cr@P_2Si has a bandgap of 1.451 eV. Therefore the possibility of Sc, Cr and Mn atoms as electrocatalysts is ruled out. It is worth noting that V@P_2Si has a bandgap of only 0.322 eV, together with the structurally stable results demonstrated by molecular dynamics data, we therefore next focus on the application of V@P_2Si in the electrochemical catalytic reduction of CO_2.

For monoatomic catalysts, the inability of the metal atoms to achieve dispersion on the catalyst as a single atom and thus be uniformly and stably embedded on the monolayer, rather than agglomerated into clusters, is key to the preparation of monoatomic catalysts. The more tightly bound the metal atoms are to the P_2Si monolayer the more difficult it is for them to migrate across the monolayer, and the more stable they proved to be. We, therefore, calculated the migration energy barriers of the four metal atoms, namely Sc, Mn, Cr and V, on the P_2Si monolayer (Fig. S5 in Supporting information). Although the migration of Sc, V and Mn atoms on the P_2Si monolayer is exothermic (between −0.38 eV and −0.20 eV) the energy barriers to be overcome are relatively high, between 1.35 eV and 2.17 eV, which can be considered as difficult for the metal atoms to overcome at room temperature to migrate. The migration of the V atom is thermally absorbing (0.56 eV) and has a high energy barrier (around 1.70 eV). The initial, transition and final states of the four metal atoms migrating on the P_2Si monolayer are shown in Fig. S6 (Supporting information). It can be seen that the positions of metal atoms in the transition states are all in the bridge positions of the two P atoms. Therefore, M@P_2Si (M = Sc, Cr, Mn, V) are fairly stable single-atom catalysts in terms of the migration energy barriers of the metal atoms on the P_2Si monolayer, and these metal atoms can be uniformly and stably embedded on the P_2Si monolayer without forming clusters or migrating freely.

For the electrocatalytic reduction of CO_2, it is essential that the CO_2 molecule can be stably adsorbed and that the C=O bond is activated. We therefore next investigated the adsorption of CO_2 molecules by the M@P_2Si structures as shown in Fig. S7 (Supporting information). CO_2 is thermodynamically stable and kinetically inert [66], so activation of CO_2 is very difficult. As shown in Fig. 3a, the Cr and Mn atoms have the greatest effects on the bond angles of CO_2 molecules, corresponding to 143.9° and 149.75° after activation, respectively. Other metal atoms also indicate an activating effect on the CO_2 molecule but are not as strong as the first two. In terms of adsorption distances, Sc, V, Cr and Mn atoms have a stronger effect on CO_2 adsorption with adsorption distances ranging from 2.017 Å to 2.230 Å. The effects of different transition metal atoms on the adsorption energy and C=O bond length of CO_2 molecules are illustrated in Fig. 3b.

The most significant effects on C=O can be seen for M atoms (M = Mn, Cr and V), for which corresponding C=O bond lengths are 1.246, 1.270 and 1.787 Å and adsorption energies are −1.11, −1.10 and −0.70 eV, respectively. Since the adsorption energies of Ti, Fe, Co, Ni and Cu atoms for CO_2 molecules are relatively small, they proved to be unsuitable as electrocatalysts. The variation of the overall CO_2 charge and the charge of some atoms are shown in Fig. 3c. Cr@P_2Si is still the most activated single-atom catalyst for CO_2, with a charge of −0.26 e after CO_2 adsorption and the O-atom point the most electron-deficient at 0.18 e. However, its bandgap (1.45 eV) for the Cr@P_2Si doped system is not conducive to electron conduction and it is therefore also unsuitable as an electrocatalyst. The most stable structures of M@P_2Si (M = Sc-Cu) for CO_2 adsorption are illustrated in Fig. S7. Corresponding bond angles, bond lengths, and adsorption distances for CO_2 adsorption are labeled on the graph. The effects of different types of single-atom catalysts on the bond lengths and bond angles of CO_2 during CO_2 molecule activation can be seen more visually in the figure.

To investigate the intrinsic mechanism of activation of CO_2 molecule by M@P_2Si (M = Sc, Cr, Mn, V), we studied the charge density difference (CDD), the electron localization function (ELF), and the partial density of states (PDOS) of the adsorption structure, as shown in Figs. S8 and S9 (Supporting information). The yellow region between CO_2−Mn has the largest volume, indicating that the binding strength of CO_2−Mn is greater than that of CO_2-Sc, CO_2-V and CO_2-Cr, which also corresponds to the largest adsorption energy −1.22 eV of CO_2 adsorption for the Mn@P_2Si. This corresponds to the highest number of electrons transferred by the Cr@P_2Si material to the CO_2 molecule (−0.260 e).

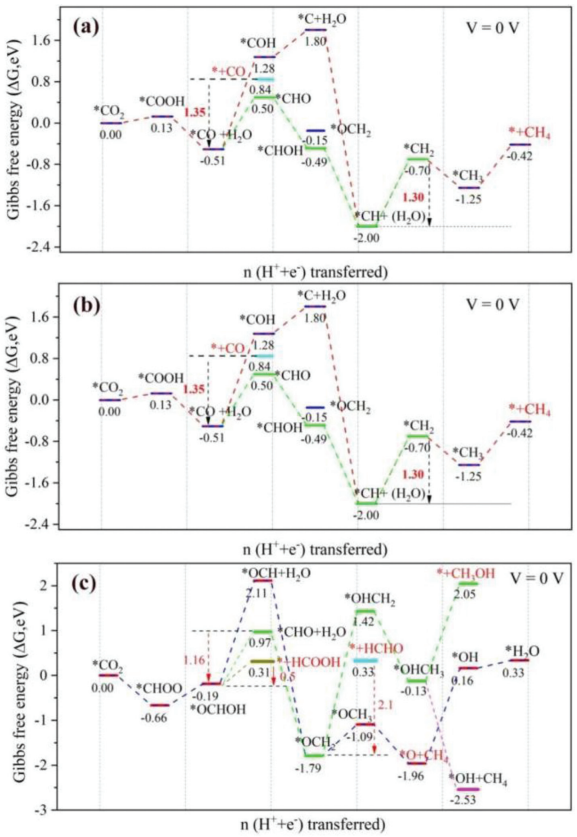

Fig. 3. (a–c) The Gibbs free energy distributions for the most suitable path of CRR for V@P_2Si at an applied voltage of 0 (*vs.* RHE). The free energy change for the decisive velocity step is 0.5 eV (*OCHOH→*+HCOOH).

The distribution of electrons and the electronic contribution of the M@P_2Si catalyst to CO_2 can be seen in the ELF diagram in Fig. S8. The density of states data in Fig. S9 show the enhanced interaction due to the greater overlap between the 3d orbital of the metal atoms and the 2p orbital of $*CO_2$. It is noteworthy that more electrons leap into lower energy levels after CO_2 adsorption, indicating the formation of a more stable adsorption structure. It can also be noted that spin states of the Mn and V atoms are asymmetrically indicating the presence of magnetism, but Cr and Sc atoms have no magnetic moments. 3d orbitals of Sc atom are the strongest for CO_2, corresponding to its electron leap of $*CO_2$ into deeper energy levels.

We calculated the entire electrochemical reduction of the CO_2 molecule and all possible intermediates in the process. The first thing that had to be considered is the competition between CRR and HER [67]. This is because, at each hydrogenation step in the CRR process, a proton-electron pair ($H^+ + e^-$) takes part in the reaction [68]. For the first hydrogenation step, the hydrogen addition may be on the C-atom of the CO_2 molecule or the O-atom end, going through $* + CO_2 + H^+ + e^- \rightarrow$ *COOH or $* + CO_2 + H^+ + e^- \rightarrow$ *CHOO to obtain two different mid-shelf bodies. However, since the reduction reaction takes place in an acidic solution, the active site can accept proton-electron pairs in addition to CO_2 hydrogenation to obtain *H, which is then further hydrogenated to obtain gaseous H_2 that is desorbed from the surface of the active site, which is known as the hydrogen precipitation reaction (HER) [69]. It is, therefore, necessary to discuss the competition between CRR and HER, with the results shown in Fig. 4. A comparison of the

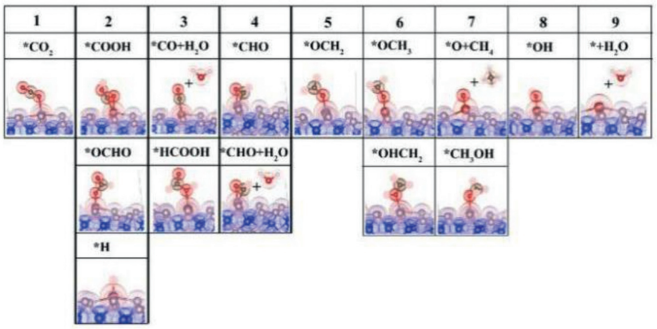

Fig. 4. Side views of the structure of the key intermediate for the electrochemical reduction of CO_2. The first row of numbers is the number of proton-electron pairs transferred to the CO_2 molecule in the reaction.

free energy change between CRR and HER first-step hydrogenation shows that, except for Mn@P_2Si where ΔG_{*COOH} is greater than ΔG_{*H}, the ΔG_{*COOH} and ΔG_{*CHOO} of the remaining metal-atom modified single-atom catalysts are smaller than the corresponding ΔG_{*H}, indicating that it is easier to form *COOH and *CHOO than to form *H first-step protonation. Because the metal active site on the monolayer for the catalyst is limited, so once the active site is occupied by *CHOO or *COOH, there will be no spare active site for the HER reaction, and therefore M@P_2Si (M = Sc, V, Cr) has good CRR selectivity. It is noteworthy that for V@P_2Si catalysts ΔG_{*CHOO} is less than ΔG_{*COOH}, so it is thought that for V@P_2Si its first step of protonation prefers the formation of *CHOO intermediates.

Next, we consider the protonation of *COOH or *OCHO by assessing the free energy of further reduction intermediates (Fig. 3). Fig. 4 shows a schematic structure of the key intermediates in the most suitable CRR reaction pathway. Given the wide variety of products in the CRR pathway, we next determined the optimal reaction pathway and the main reduction products by comparing the change in Gibbs free energy of protonation at each step and the magnitude of the P_2Si adsorption energy of the products [70]. The intermediates obtained from the first step of hydrogenation in CRR are *COOH and *CHOO, and if the protonation of *COOH continues it will undergo $^*COOH + H^+ + e^- \rightarrow {}^*CO + H_2O \rightarrow {}^* + CO$ to give the product carbon monoxide (CO). In contrast, *CHOO undergoes $^*CHOO + H + e^- \rightarrow O^*CHOH \rightarrow {}^* + HCOOH$ to obtain the product formic acid (HCOOH). Whether the CO and HCOOH obtained can be desorbed from the P_2Si monolayer depends on the size of the adsorption energy, if the adsorption energy is small then it can be desorbed from the SACS surface and vice versa it is further protonated. As shown in Fig. 3, it is energetically easier to form *CHOO and then further hydrogenates to form *OCHOH, but HCOOH has adsorption energy of −0.28 eV which is easier to desorb and therefore energetically more favorable to formic acid (HCOOH). The most suitable reaction pathway for CRR is, therefore, $^*CO_2 \rightarrow {}^*CHOO \rightarrow O^*CHOH \rightarrow {}^* + HCOOH$, with the final reduction product being HCOOH. In addition, we have calculated all other possible pathways in Fig. 3, which shows all the possibilities for the CRR.

The overpotential is an important parameter in assessing the performance of a catalyst [71]. To achieve high reactivity and selectivity for CO_2 reduction, the catalyst should have a relatively large negative limiting potential. From the formulae used to calculate the details, it is clear that a larger negative limit potential corresponds to a smaller overpotential. In the V@P_2Si-catalyzed CO_2 reduction process, where the potential decisive step is $^*OCHOH \rightarrow {}^*$+HCOOH, the limited potential is −0.5 V (*vs.* RHE), and the overpotential is 0.75 V (*vs.* RHE), respectively.

In conclusion, we predicted a P_2Si monolayer using the CALYPSO package, and the stabilities were examined *via* formation energy, mechanical criteria, MD simulations, and phonon dispersion first. The P_2Si monolayer is a semimetal with a band gap of 0.0047 eV at the GGA-PBE level or metal for HSE06 hybrid functional. We further focus on transition metal single-atom catalysts (TSACs) as potential CO_2 electroreduction catalysts, and the best performing V@P_2Si was screened by using the bandgap change after metal atom doping. The activation ability of the SACs towards CO_2, the migration potential of metal atoms on the P_2Si monolayer, molecular dynamics simulation stability assessment, and comparing the Gibbs free energy change for the first protonation step of CRR and HER were studied and discussed, showing that the V@P_2Si has good CRR selectivity rather than hydrogen production. Especially in the V@P_2Si-catalyzed CO_2 reduction process, where the potential decisive step (PDS) is $^*OCHOH \rightarrow {}^*$+HCOOH, the limiting potential is −0.5 V (*vs.* RHE) and the overpotential is 0.75 V (*vs.* RHE). Our theoretical calculations predict that the P_2Si monolayer is a potential 2D material in nanoelectronics, and V-modified P_2Si monolayers are expected to be ideal as novel single-atom catalysts for the electrocatalytic reduction of CO_2.

Declaration of competing interest

The authors declare that they have no known competing financial interests or personal relationships that could have appeared to influence or personal relationships that could have appeared to influence the work reported in this paper.

Acknowledgments

This study was funded by the Natural Science Foundation of China (Nos. 21603109, 11304128), the Henan Joint Fund of the National Natural Science Foundation of China (No. U1404216), the Science and Technology Program of Henan Department of Science and Technology, China (No. 182102310609), and the Construct Program of Applied Characteristic Discipline in Hunan University of Science and Engineering (Mathematics, Education and Electronic Science and Technology).

Supplementary materials

Supplementary material associated with this article can be found, in the online version, at doi:10.1016/j.cclet.2022.06.002.

References

[1] K.S. Novoselov, A.K. Geim, S.V. Morozov, et al., Science 306 (2004) 666–669.
[2] X. Zhang, Y. Xie, Chem. Soc. Rev. 42 (2013) 8187–8199.
[3] L. Li, Y. Yu, G.J. Ye, et al., Nat. Nanotechnol. 9 (2014) 372–377.
[4] X. Peng, Q. Wei, A. Copple, Phys. Rev. B 90 (2014) 085402.
[5] H. Liu, A.T. Neal, Z. Zhu, et al., ACS Nano 8 (2014) 4033–4041.
[6] Z.W. Teng, C.S. Liu, X.H. Yan, Nanoscale 9 (2017) 5445–5450.
[7] M.C. Watts, L. Picco, F.S. Russell-Pavier, et al., Nature 568 (2019) 216–220.
[8] Y. Du, J. Zhuang, J. Wang, et al., Sci. Adv. 2 (2016) e1600067.
[9] J.G. Keizer, S. Koelling, P.M. Koenraad, et al., ACS Nano 9 (2015) 12537–12541.
[10] B. Huang, H.L. Zhuang, M. Yoon, et al., Phys. Rev. B 91 (2015) 121401.
[11] X. Fu, H.Y. Yang, L. Fu, et al., Chin. Chem. Lett. 32 (2021) 1089–1094.
[12] T.L. Chan, M.L. Tiago, E. Kaxiras, et al., Nano Lett. 8 (2008) 596–600.
[13] K. Sato, A. Castaldini, N. Fukata, et al., Nano Lett. 12 (2012) 3012–3017.
[14] T.E. Park, B.C. Min, I. Kim, et al., Nano Lett. 11 (2011) 4730–4735.
[15] N.J. Kramer, K.S. Schramke, U.R. Kortshagen, Nano Lett. 15 (2015) 5597–5603.
[16] K.J. Dykema, T.N. Truong, M.S. Gordon, J. Am. Chem. Soc. 107 (1985) 4535–4541.
[17] Y. Wang, M. Miao, J. Lv, et al., J. Chem. Phys. 137 (2012) 224108.
[18] H. Wang, Y. Wang, J. Lv, et al., Comput. Mater. Sci. 112 (2016) 406–415.
[19] G.P. Li, Z.Z. Li, H.F. Xie, et al., Chin. J. Struct. Chem. 40 (2021) 1047–1054.
[20] S.H. Liu, Y. Li, K.N. Ding, et al., Chin. J. Struct. Chem. 39 (2020) 2068–2076.
[21] H. Yang, Y. Wu, G. Li, et al., J. Am. Chem. Soc. 141 (2019) 12717–12723.
[22] S. Zhou, M. Wang, S. Wei, et al., Mater. Today Phys. 16 (2021) 100301.
[23] C. He, R. Wang, D. Xiang, et al., Appl. Surf. Sci. 509 (2020) 145392.
[24] H. Yang, C. He, L. Fu, et al., Chin. Chem. Lett. 32 (2021) 3202–3206.
[25] Q. Li, Y.C. Wang, J. Zeng, et al., Rare Met. 40 (2021) 3442–3453.
[26] N. Sathishkumar, S.Y. Wu, H.T. Chen, Chem. Eng. J. 391 (2020) 10.
[27] X. Liu, S. Wei, S. Zhou, et al., J. CO_2 Util. 26 (2018) 588–594.

[28] Y. Wang, Z. Huang, Y. Lei, et al., Chem. Commun. 58 (2022) 3621–3624.
[29] Y. Wang, Y. Liu, W. Liu, et al., Energ. Environ. Sci. 13 (2020) 4609–4624.
[30] R. Cheng, C.C. Chung, S. Wang, et al., Mater. Today Phys. 17 (2021) 100358.
[31] S. Zhou, M. Wang, S. Wei, et al., Mater. Today Phys. 21 (2021) 100539.
[32] D. Liu, Y. Liu, M. Li, J. Phys. Chem. C 124 (2020) 6145–6153.
[33] L. Fu, R. Wang, C. Zhao, et al., Chem. Eng. J. 414 (2021) 128857.
[34] B. Yang, L. Li, Z. Jia, et al., Chin. Chem. Lett. 31 (2020) 2627–2633.
[35] R.G. Zhang, G.R. Wang, B.J. Wang, J. Catal. 305 (2013) 238–255.
[36] Q.G. Jiang, Z.M. Ao, S. Li, et al., RSC Adv. 4 (2014) 20290–20296.
[37] Y. Wang, L. Xu, L. Zhan, et al., Nano Energy 92 (2022) 106780.
[38] A. Pekkari, Z. Say, A. Susarrey-Arce, et al., ACS Appl. Mater. Interfaces 11 (2019) 36196–36204.
[39] X. Xu, S. Wang, S. Guo, et al., Adv. Powder Mater. (2021) 100027.
[40] C. Liu, Q. Li, J. Zhang, et al., J. Mater. Chem. A 7 (2019) 4771–4776.
[41] Y. Liu, Q. Feng, W. Liu, et al., Nano Energy 81 (2021) 105641.
[42] R. Kumar, M. Kumar, Rare Met. 39 (2020) 1110–1112.
[43] Y.F. Zhang, Y.K. Zhu, C.X. Lv, et al., Rare Met. 39 (2020) 841–849.
[44] G. Kresse, D. Joubert, Phys. Rev. B 59 (1999) 1758–1775.
[45] J.P. Perdew, K. Burke, M. Ernzerhof, Phys. Rev. Lett. 77 (1996) 3865–3868.
[46] G. Kresse, J. Furthmüller, Phys. Rev. B 54 (1996) 11169–11186.
[47] G. Kresse, J. Furthmüller, Comput. Mater. Sci. 6 (1996) 15–50.
[48] J. Paier, M. Marsman, K. Hummer, et al., J. Chem. Phys. 125 (2006) 249901.
[49] A. Togo, I. Tanaka, Scr. Mater. 108 (2015) 1–5.
[50] B. Delley, J. Chem. Phys. 113 (2000) 7756–7764.
[51] B. Delley, J. Chem. Phys. 92 (1990) 508–517.
[52] A. Klamt, G. Schüürmann, J. Chem. Soc. Perkin (1993) 799–805.
[53] J. Rossmeisl, A. Logadottir, J.K. Nørskov, Chem. Phys. 319 (2005) 178–184.
[54] S. Liu, B. Liu, X. Shi, et al., Sci. Rep. 7 (2017) 2404.
[55] H. Wang, X. Li, J. Sun, et al., 2D Mater. 4 (2017) 045020.
[56] D. Fan, S. Lu, Y. Guo, et al., J. Mater. Chem. C 6 (2018) 1651–1658.
[57] Y. Wang, M. Qiao, Y. Li, et al., Nanoscale Horiz. 3 (2018) 327–334.
[58] Q. Peng, X. Wen, S. De, RSC Adv. 3 (2013) 13772–13781.
[59] Y. Cai, G. Zhang, Y.W. Zhang, J. Am. Chem. Soc. 136 (2014) 6269–6275.
[60] B. Rajbanshi, P. Sarkar, J. Phys. Chem. Lett. 8 (2017) 747–754.
[61] Y. Zhou, Z. Wang, P. Yang, et al., ACS Nano 6 (2012) 9727–9736.
[62] B. Radisavljevic, A. Radenovic, J. Brivio, et al., Nat. Nanotechnol. 6 (2011) 147–150.
[63] M. Li, H. Wang, W. Luo, et al., Adv. Mater. 32 (2020) 2001848.
[64] M. Wang, Z. Zhang, Y. Gong, et al., Appl. Surf. Sci. 502 (2020) 144067.
[65] W. Luc, B. Ko, S. Kattel, et al., J. Am. Chem. Soc. 141 (2019) 9902–9909.
[66] B.M. Tackett, E. Gomez, J.G. Chen, Nat. Catal. 2 (2019) 381–386.
[67] D.R. Yang, L. Liu, Q. Zhang, et al., Sci. Bull. 65 (2020) 796–802.
[68] A. Liu, J. Long, S. Yuan, et al., Phys. Chem. Chem. Phys. 21 (2019) 5133–5141.
[69] F. Chekin, S. Bagheri, S. Bee Abd Hamid, J. Chin. Chem. Soc. 60 (2013) 447–451.
[70] J. Noh, S. Back, J. Kim, et al., Chem. Sci. 9 (2018) 5152–5159.
[71] J. Kothandaraman, A. Goeppert, M. Czaun, et al., J. Am. Chem. Soc. 138 (2016) 778–781.